BULLETIN OF THE POLISH ACADEMY OF SCIENCES
TECHNICAL SCIENCES, Vol. 64, No. 2, 2016
DOI: 10.1515/bpasts-2016-0048

Experimental and numerical analysis of shunting effect in resistance spot welding of Al2219 sheets

M. JAFARI VARDANJANI[1]*, A. ARAEE[2], J. SENKARA[3], J. JAKUBOWSKI[3] and J. GODEK[3]

[1]Department of Welding Engineering, Warsaw University of Technology, Poland
[2]Department of Mechanical Engineering, University of Tehran, Iran, Postal address: Kuy-e-Daneshgah, 14395-515 Tehran, Iran
[3]Department of Welding Engineering, Warsaw University of Technology, Poland, Postal address: Narbutta 85 St., 02-524 Warsaw, Poland

Abstract. Few aspects of shunting effect have been studied so far. Shunting effect in resistance spot welding (RSW) occurs when the electrical current passes through the previous spot welds. Value of this current depends mostly on distance, number, and size of previous spot welds. This will cause some dimensional and metallurgical changes in welding nugget as well as heat affected zone (HAZ). In this study, shunting effect of RSW is considered by finite element method (FEM) and the results are compared to experiments performed on aluminum alloy 2219. Weld spacing together with welding current and time are considered to discover the effect of shunting current in the final quality of nugget. A three factor experiment design has been performed to find the significance of factors and interactive effects, as well as finite element model verification. Electrothermal and mechanical interactions are considered in the FEM. Experimental and numerical solutions have yielded similar results in terms of welding nugget properties. Asymmetry in electrical potential, temperature, stress distribution and geometry of shunted nugget is predicted and verified directly or indirectly. Intense effect of shunting current on nugget height, asymmetric growth of heat affected zone (HAZ) toward previous welding nugget, as well as concentration of alloying elements along grain boundaries are also discovered.

Key words: resistance spot welding, shunting, finite element analysis, experiment.

1. Introduction

Few studies can be found on shunting effect, however, most resistance spot welding (RSW) applications comprise multiple spots. Intermittent spots change the mechanical and metallurgical quality of new spot due to thermal-electrical alternations caused by shunting current, passing via the previous spot(s). This proves the necessity of shunting effect analysis to optimize the adjustable parameters and compensate undesirable consequences.

The oldest experimental study of shunting effect was performed by Hard et al. [1] They provided a method for shunting path detection. Next studies [2] investigated the effect of sheet dimensions, welding distance, electrode geometry, material, and electrode force in order to find minimum required distance to reduce shunting effect. Howe [3] and Wang et al. [4] tested several types of steels and discovered the dominant effect of distance and surface conditions in shunting intensity. Senkara [5] and Zhang [6] considered mechanical aspects of shunting effect on crack generation in RSW of AA5754. Although shunting current was claimed to be efficient in crack generation, deeper investigation seems to be required to discover the effect of other parameters such as distance. In the simplified 3D electrothermal finite element model designed by Chang [2], voltage and temperature distributions were predicted for a shunted nugget. In the theoretical model developed by Li et al. [7], minimum required distance was obtained, however it was mainly based on several geometrical and mathematical simplifications.

Finite element models used to analyze RSW process are not readily usable to consider shunting effect, however, there are several RSW FEM studies on simulation of thermal and electrical distribution (Huh [8], Archer [9], Greenwood [10], and Tsai [11]), prediction of the electrical and thermal contact properties and contact radius (Loulou et al. [12], Okuda [9], and Shen et al. [13]), growth of nugget and thermal deformations (Nied [14], Gould [15]), and electrical-thermal-mechanical analysis (Zhang [16] and Kim et al. [17]). Although most of these studies have included thermal, electrical and mechanical aspects of the RSW process, the asymmetry of shunting configuration due to existence of shunting (previous) nugget prohibits the use of 1D or 2D axisymmetric models.

In this paper, shunting effect in RSW is investigated using FEM and the results are compared with experiments on AA2219. The influence of welding distance, current and time are investigated to consider shunting effect in final quality of the nugget. Experiments are designed inside the weldability range, while the results are compared to results of FEM after verification.

2. Methods

2.1. Finite Element Analysis

2.1.1. Mathematical Equations

2.1.1.1. Electrical equations

Quasi-Laplace equation of electrical potential is written in 3D coordinates as [1]:

$$\frac{\partial}{\partial x}\left[\frac{1}{\rho}\cdot\frac{\partial \phi}{\partial x}\right]+\frac{\partial}{\partial y}\left[\frac{1}{\rho}\cdot\frac{\partial \phi}{\partial y}\right]+\frac{\partial}{\partial z}\left[\frac{1}{\rho}\cdot\frac{\partial \phi}{\partial z}\right]=0\,, \qquad (1)$$

*e-mail: mehdijafari@ut.ac.ir

where ϕ is the voltage potential and ρ is the bulk electrical resistivity. Boundary conditions are provided in Table 1 according to Fig. 1. In Table 1, ϕ_e is the voltage applied on electrode, ρ_{ES} is the electrical contact resistivity between the electrode and sheet, $\Delta\phi_{SS}$ is the voltage drop between the sheets, ρ_{SS} is the electrical contact resistivity between the weldments, and $\Delta\phi_{Sh}$ is the voltage drop in shunting nugget. For the application of the alternative current it can be assumed that [18]:

Table 1
Electrical boundary conditions

Boundary	Equation	
Electrode-sheet Interface [2]	$\frac{1}{\rho}\left(\frac{\partial\phi}{\partial z}\right)=\frac{1}{\rho_{ES}}(\phi_e-\phi)$	(2)
Faying surface [2]	$\frac{1}{\rho}\left(\frac{\partial\phi}{\partial z}\right)=\frac{1}{\rho_{SS}}(\Delta\phi_{SS})$	(3)
Surfaces exposed to ambient	$\frac{1}{\rho}\left(\frac{\partial\phi}{\partial z}\right)=0$	(4)
Perimeter of shunting nugget	$\frac{1}{\rho}\left(\frac{\partial\phi}{\partial z}\right)=\frac{1}{\rho_{Sh}}(\Delta\phi_{Sh})$	(5)

$$I_e=\frac{I_p}{\sqrt{2}}, \tag{6}$$

where I_e is the applied eletrical current on electrode and I_p is the maximum electrical current supplied in welding machine. The following equation is used to calculate electrical contact resistivity [18]:

$$\rho_C(T)=R_C(20°C)\cdot\frac{A_C}{L_C}\sqrt{\frac{\sigma_{e,ave}(T)}{\sigma_{e,ave}(20°C)}}, \tag{7}$$

where $R_c(20°C)$ is the measured electricl contact resistance (ECR) of electrode-sheet interface at 20°C under constant mechanical pressure, L_c is the characteristic thickness of contact surfaces (assumed equal to 1×10^{-4} for certain aluminum alloys as reported by Sun [19]), A_c is nominal contact area, and $\sigma_{e,ave}(T)$ and $\sigma_{e,ave}(20°C)$ are the average yield stress of contacting materials at T and 20°C, respectively.

2.1.1.2. Thermal equations. Thermal equation is presented in (8) [2].

$$D\cdot c\cdot\frac{\partial T}{\partial t}=\frac{\partial}{\partial x}\left[k\cdot\frac{\partial T}{\partial x}\right]+\frac{\partial}{\partial y}\left[k\cdot\frac{\partial T}{\partial y}\right]+\frac{\partial}{\partial z}\left[k\cdot\frac{\partial T}{\partial z}\right]+\frac{1}{\rho}\nabla\phi\cdot\nabla\phi\,, \tag{8}$$

where D is mass density, c is specific heat capacity, k is thermal conductivity coefficient, T is temperature, and ϕ is voltage. Specific heat capacity at melting temperature is given by (9) [20].

$$c'=c_{T_s}+\frac{H_m}{T_s}, \tag{9}$$

where H_m is the latent heat (Heat of fusion), T_s is the temperature at which the melting starts, C_{T_s} is the specific heat at T_s, and c' is the specific heat capacity after phase change. Thermal boundary conditions are provided in Table 2, where k_{ES} and k_{SS} are thermal contact conductivity (TCC) coefficients of electrode-sheet interface and sheets, respectively, k_e is thermal conductivity coefficient of electrode, T_W and T_A are water and ambient temperature, respectively, h_W and h_A are thermal convection coefficient of water and ambient, respectively, and n is surface normal vector. TCC coefficients are calculated using (15) as reported by Zhang and Senkara [21].

Table 2
Thermal boundary conditions

Boundary	Equation	
Contact surface of electrode and sheet [2]	$-k_{ES}\frac{\partial T}{\partial z}=\frac{1}{\rho_{ES}}(\phi-\phi_e)^2$	(10)
Faying surface [2]	$-k_{SS}\frac{\partial T}{\partial z}=\frac{1}{\rho_{SS}}(\Delta\phi)^2$	(11)
Inside electrode exposed to water	$-k_e\frac{\partial}{\partial z}T=h_W(T-T_W)$	(12)
Sheet exposed to ambient	$-k\frac{\partial}{\partial z}T=h_A(T-T_A)$	(13)
Unspecified surfaces	$\frac{\partial T}{\partial n}=0$	(14)

$$k_c=\frac{1}{3}\left(\frac{\sigma}{\sigma_e}\right)\left(\frac{k_1+k_2}{2}\right), \tag{15}$$

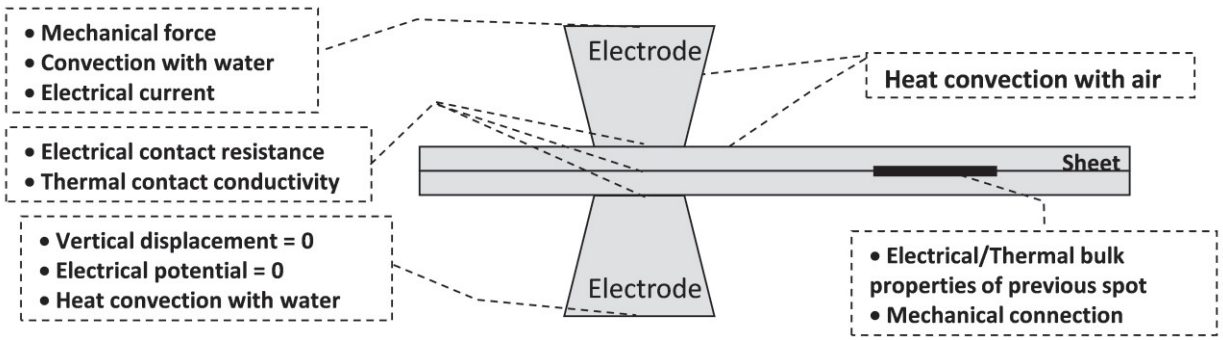

Fig. 1. Schematics for boundary conditions and important domains

where k_c is TCC coefficient, σ is normal stress, σ_e is yield stress, and k_1 and k_2 are TCC coefficients of contacting parts.

2.1.1.3. Mechanical equations. Incremental elastic-plastic equation is used for thermal-mechanical solution [22].

$$d\{\sigma\} = [C]d\{\epsilon\} - \{C_T\}dT, \tag{16}$$

where $d\{\sigma\}$ and $d\{\epsilon\}$ are stress and strain vector differences, respectively, $[C]$ is elastic-plastic matrix, $\{C_T\}$ is thermal coefficient vector, and dT is temperature difference. Stress equilibrium is governed using the following equation:

$$\nabla\{\sigma\}_{xyz} + D \cdot \{b\} = D.\{a\}, \tag{17}$$

where $\{b\}$ and $\{a\}$ are body force and acceleration vectors respectively [22]. Mechanical boundary conditions are provided in Table 3 according to Fig. 1. In Table 3, F_E is electrode force, and A_{ES} is contacting area between electrode and weldment. Shunting and welding domains are not considered as free surfaces in (20).

Table 3
Mechanical boundary conditions

Boundary	Equation	
Top of the upper electrode [22]	$\sigma_z = \frac{F_E}{A_{ES}}$	(18)
Bottom of the lower electrode	$\frac{\partial z}{\partial t} = 0$	(19)
Free surfaces of the weldments	$\sigma_z = 0$	(20)

2.1.2. Configuration of the model. To simplify the calculation process, the previous nugget is defined as a cylindrical connection between the sheets (Fig. 2) and the diameter is specified according to the dimensions of an experimental nugget, obtained using average welding parameters in single spot welding.

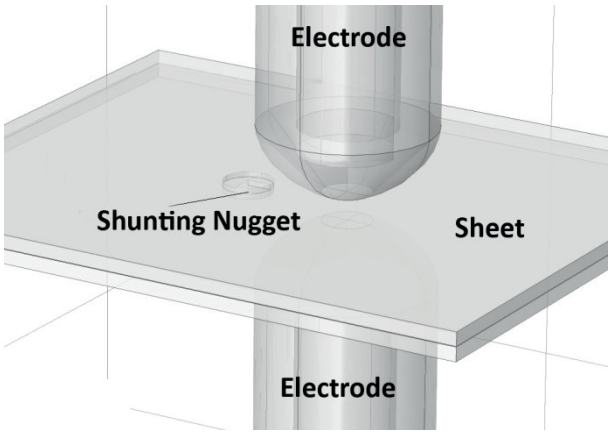

Fig. 2. Welding configuration, showing shunting nugget and other parts in FEM model

2.1.3. Material properties. Elastic-plastic material is specified as the type of material for AA2219 (sheets) in the model. Table 4 provides important temperature-dependent properties of AA2219, while solidus and liquidus temperatures are set at 543 and 643°C respectively [23] and fusion heat is assumed 389 kJ/kg [24]. Table 5 and 6 provide chemical composition and important properties of C15000 (electrodes), respectively.

Table 4
Different material properties for AA2219–T6 as a function of temperature

Parameter	Function	
Density (kg/m^3) [23]	$D(T) \cong 0.0002\times T^2 - 0.17\times T + 2858.3$	(21)
Electrical resistivity $(\Omega.m)$ [24]	$\rho(T) = 5.7 \times 10^{-8} \times (1 + 0.0017 \times (\mathrm{T} - 293))$	(22)
Linear thermal expansion $(1/K)$ [23]	$\alpha(T) \cong (0.0063 \times T + 19.708) \times 10^{-6}$	(23)
Specific heat capacity (J/(kg.K)) [25]	$c(T) \cong -0.0016T^2 + 1.3521T + 567.72$	(24)
Thermal Conduction Coefficient (W/(m.K)) [25]	$k(T) \cong 0.1836T + 71.847$	(25)
Elasticity Modulus (GPa) [25]	$E(T) \cong 2 \times 10^{-7}T^3 - 0.0005T^2 + 0.2253T + 43.386$	(26)
Yield Strength (MPa) [23]	$\sigma_e(T) \cong 7 \times 10^{-6}T^3 - 0.0102T^2 + 4.0876T - 129.96$	(27)

Note: T is temperature in K

Table 5
Chemical composition of C15000

Element	Percentage
Cu	99.80 to 99.85
Zr	0.15 to 0.20

Table 6
Different material properties for C15000 as a function of temperature

Parameter	Function	
Linear thermal expansion (1/K) [11]	$\alpha_E(T) \cong (3\times10^{-6}T^2 + 0.0013\times T + 15.934)\times10^{-6}$	(28)
Electrical resistivity (Ω.m) [11]	$\rho_E(T) \cong (10^{-5}T^2 + 0.0009\times T + 1.3754)\times10^{-8}$	(29)
Specific heat capacity (J/(kg.K)) [11]	$c_E(T) \cong 8\times10^{-5}T^2 + 0.0726T + 369.7$	(30)
Thermal Conduction Coefficient (W/(m.K)) [11]	$k_E(T) \cong -2\times10^{-5}T^2 - 0.1147T + 424.89$	(31)
Elasticity Modulus (GPa) [11]	$E_E(T) \cong 10^{-7}T^3 - 0.0002T^2 - 0.0516T + 150.81$	(32)
Yield strength (MPa) [11]	83	

Note: T is temperature in K

Using the method studied by Vogler [26], electrical resistivity of a single spot is measured obtaining $7.11\times10^{-8}\,\Omega.m$ and applied to the previous nugget in finite element model, while room temperature electrical and thermal properties are assigned to previous nugget since there is subtle heat generation in this domain. Elasticity modulus and yield strength were determined by performing a micro-hardness test on mounted single nugget by the method reported by Jafari et al. [27]. Electrical resistivity, elasticity modulus, and yield strength were measured obtaining 7.11×10^{-8} Ωm, 75 *GPa*, and 342 *MPa* respectively.

Applying the same method used by Vogler [26], sheets and electrode-sheet ECR were measured obtaining 6.78×10^{-5} and $8.1\times10^{-7}\,\Omega$, respectively.

2.2. Experiments. Weldability tests, design of experiment (DOE), model verification, and finding the significance of factors were the main phases of experiments. Principles of coupon preparation, inspection of results, as well as preheating and welding parameters were excerpted from military and welding handbooks [28,29]. 12 *kA* and 4 cycles[1] were chosen for preheating, while off time was 2 cycles. Squeeze and holding force were 2 and 3.2 *kN* respectively. Initial range of welding current, time, and force were 22–26 *kA*, 2–10 cycles, and 2.5–3.2 *kN*, respectively. Electrode was chosen as dome type according to previous studies [30, 31] (Fig. 3).

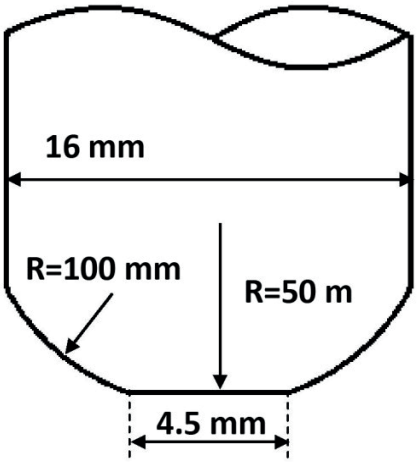

Fig. 3. Geometry of electrodes

2.2.1. Weldability tests. Weldability window was obtained (Fig. 4) after finding allowable electrode force to provide an expulsion free nugget diameter between $3.5\sqrt{t_s}$ and $5\sqrt{t_s}$ [28,32], where t_s is sheet thickness [29].

2.2.2. Significance of factors. A three factor design of experiment (DOE) was performed in a rectangular area inside the welding lobe, while welding distance range was set according to a previous study by Howe [3] (Table 7). The purpose of performing a DOE on welding parameters (factors) was to check the significance of each factor and to set new levels of those factors for next series of experiments according to the significance obtained by DOE results. Fig. 5 and 6 show schematic and real samples after welding respectively. Spot S_1 on all samples was welded using average parameters provided in Table 8. After welding procedure, the specimens were cut through the spots for geometrical and metallurgical considerations.

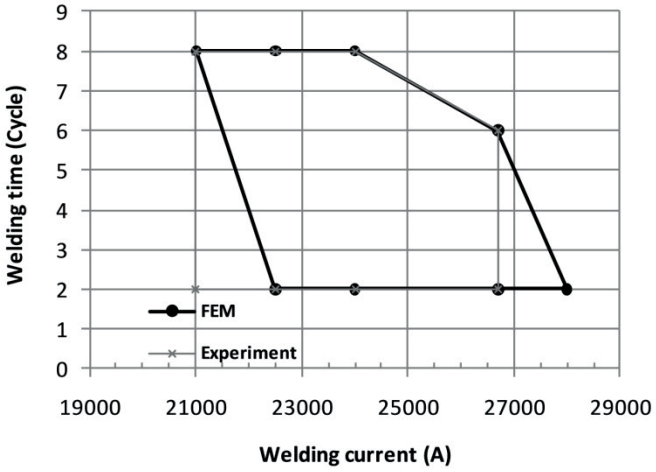

Fig. 4. Weldability region obtained by numerical and experimental results

[1]Cycles means interval between each period of 50 Hz alternative current used on welding machine.

Table 7
Chosen range of welding current and time for DOE phase

Parameter	Min	Max
Welding Current (kA)	22.5	26.7
Welding time (cycles)	2	6
Weld spacing (mm)	5	20

Table 8.
Average welding parameters for spot S_1

Current (kA)	Welding time (cycles)	Force (kN)
24	4	2.9

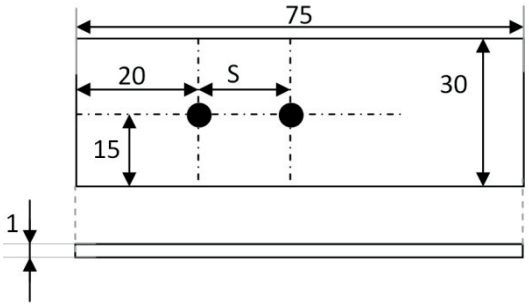

Fig. 5. Arrangement of spots for DOE; S is distance (dimensions in mm)

Fig. 6. Welded specimens

3. Results and discussion

3.1. Comparison of experimental and numerical results. Subsections explain the effect of welding current, distance, and time on nugget diameter and height – numerically and experimentally.

3.1.1. Effect of welding parameters on nugget diameter. As seen in Fig. 7, increasing welding current has increased nugget diameter while the interactive effect of welding current and distance is observed as larger current has reduced distance effect on nugget diameter growth. The main reason could be the adequacy of applied welding current to produce maximum weld nugget diameter according to the contacting area; in these circumstances, increasing distance cannot have a significant effect on the reduction of shunting effect.

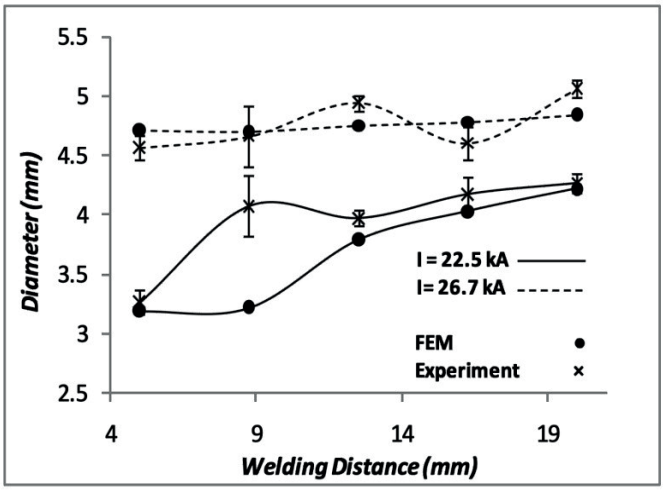

Fig. 7. Diameter-distance diagram for experimental and numerical results for 22.5 and 26.7 kA welding current, and 4 cycles welding time

Direct relationship of time and diameter can be observed in Fig. 8; however, the gradient is smaller than curves in Fig. 7, which indicates the subtle effect of time. Shunting effect can also be observed in Fig. 8, although the difference of two distances is not significant as compared to Fig. 7. Interactive effect of welding time and distance can be observed since increasing distance provides more current on contact area, therefore nugget size approaches to maximum values quickly, i.e., welding time is not capable of increasing the size significantly in long welding distances.

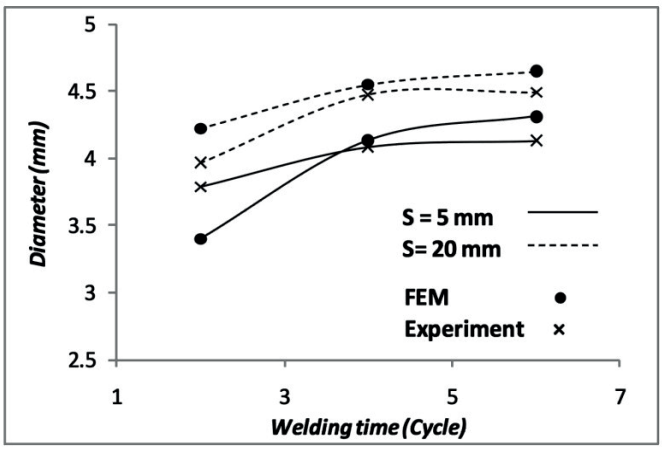

Fig. 8. Diameter-time diagram for experimental and numerical results for 5 and 10 mm welding distance, and 23.9 kA welding current

3.1.2. Effect of welding parameters on nugget height. The important difference between Fig. 9 and 7 comes from a less interactive effect of numerical results in Fig. 9. Both curves have close gradient however distance is still efficient on reduction of shunting current. Furthermore, numerical results in Fig. 9 prove the considerable effect of welding current on nugget height, as maximum height difference is about 0.8 mm.

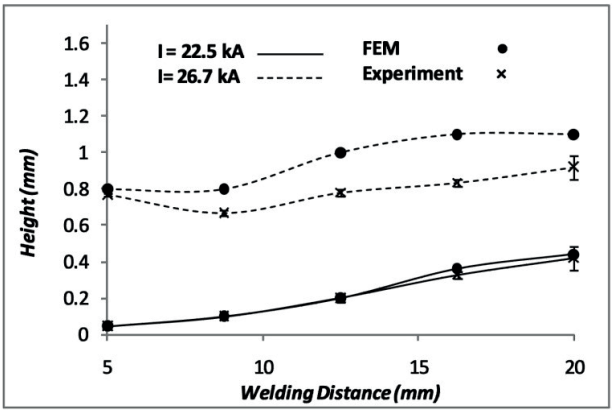

Fig. 9. Height-distance diagram for experimental and numerical results with 4 cycles welding time

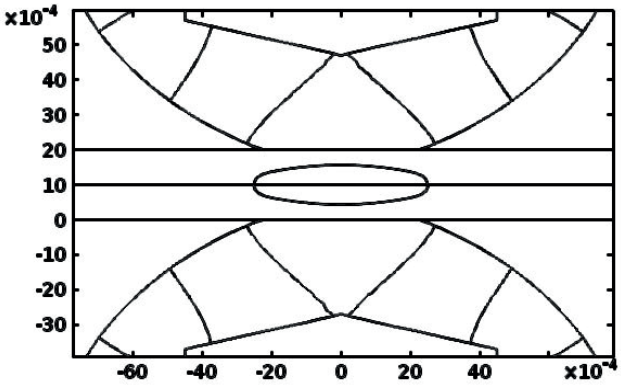

Fig. 10. Predicted equipotential lines during the application of welding current for single spot, with 25.3 kA welding current and 4 cycles welding time

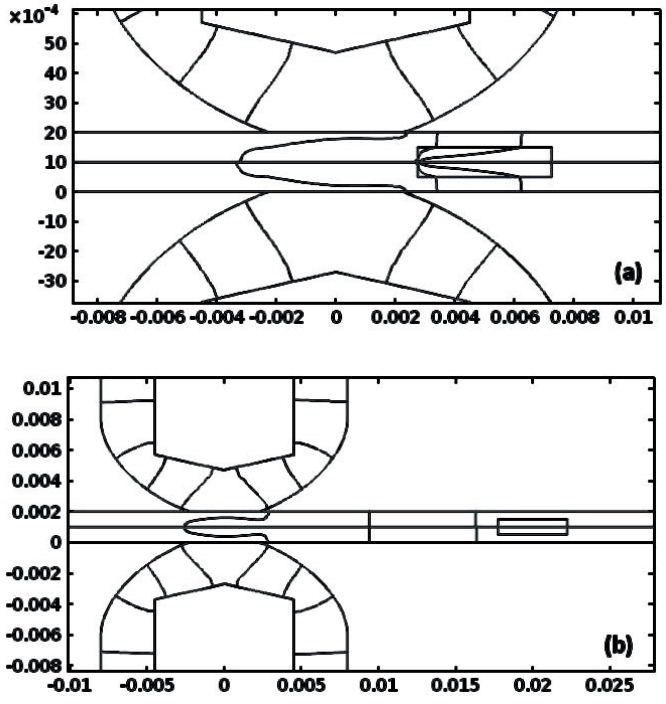

Fig. 11. Predicted equipotential lines for (a) 5 and (b) 20 mm weld spacing during the application of welding current, with 25.3 kA welding current and 4 cycles welding time, for adjacent spot welds

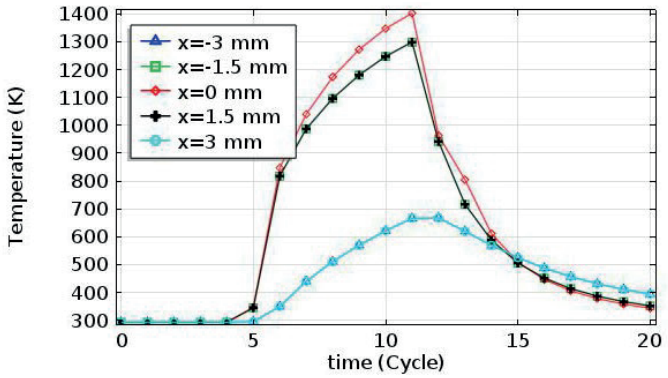

Fig. 12. Predicted cooling and heating rates at center and around the single spot weld for 25.3 kA welding current and 6 cycles welding time

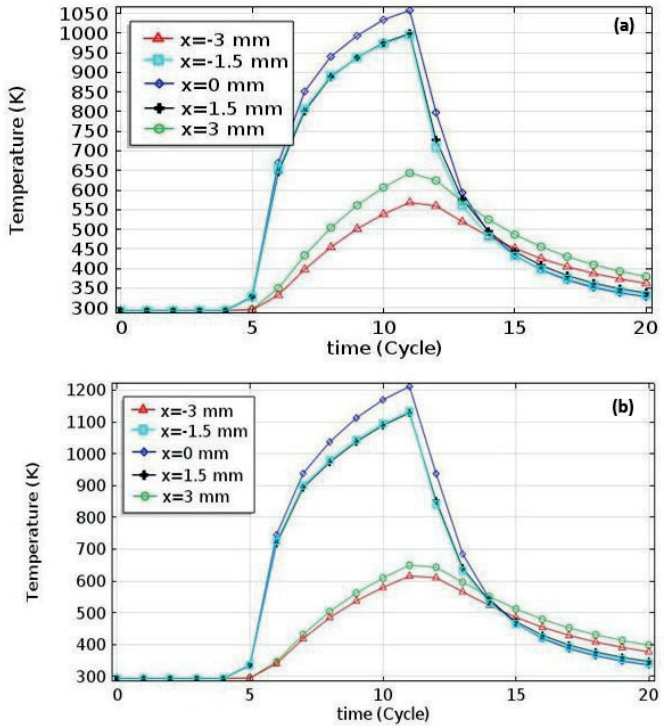

Fig. 13. Predicted cooling and heating rates for (a) 5, and (b) 20 mm welding distance, 25.3 kA welding current and 6 cycles welding at center and around the shunted spot weld (x < 0 is out of weld spacing)

3.2.1. Predicted voltage distribution. By comparing Fig. 10 and 11, the asymmetry of equipotential lines caused by shunting current is clearly observed for adjacent welding spots versus single spot. The main reason is the difference of electrical resistance between faying surface and previous spot (shunting spot). The asymmetry reduces for larger distances (Fig. 11b) due to reduction of shunting current.

3.2.2. Predicted temperature distribution. Equally distant temperature rates of HAZ locations have coincided with each other in Fig. 12 for single spot, while they are asymmetric for double spot (specially for $x = \pm 3mm$ in Fig. 13). Asymmetry of curves has decreased for longer distance (Fig. 13a and 13b). Therefore, increasing distance increases the symmetry of HAZ

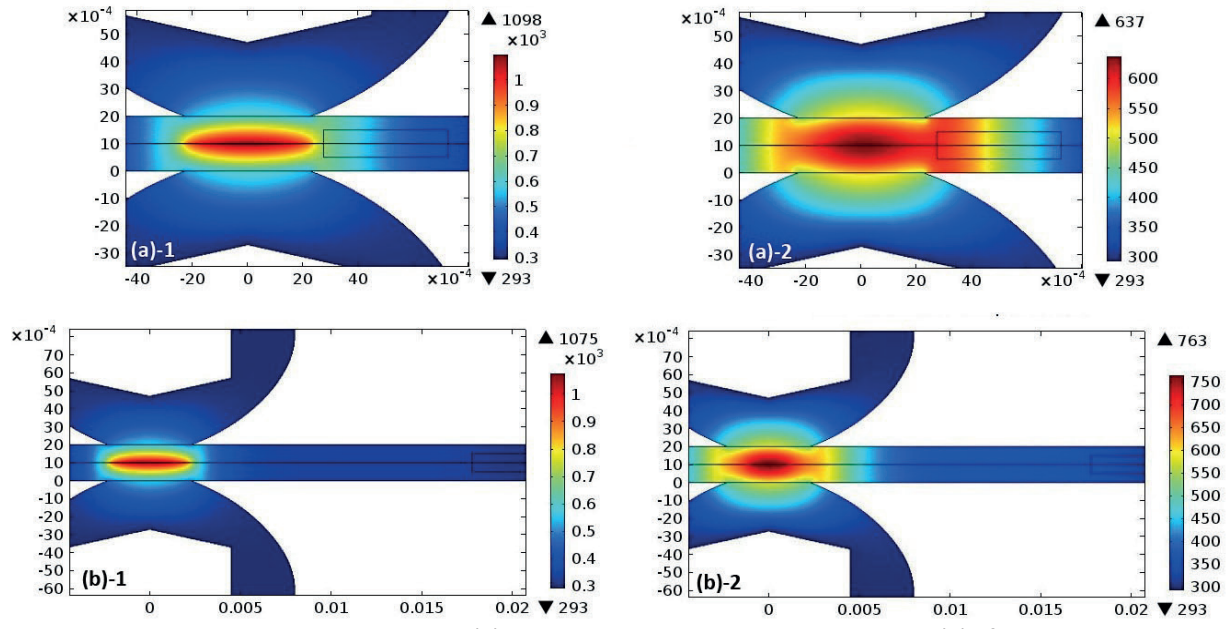

Fig. 14. Predicted temperature distribution (1) during welding current application, and (2) after removing welding current, for (a) 5, and (b) 20 mm weld spacing, with 25.3 kA welding current, in shunted spot weld

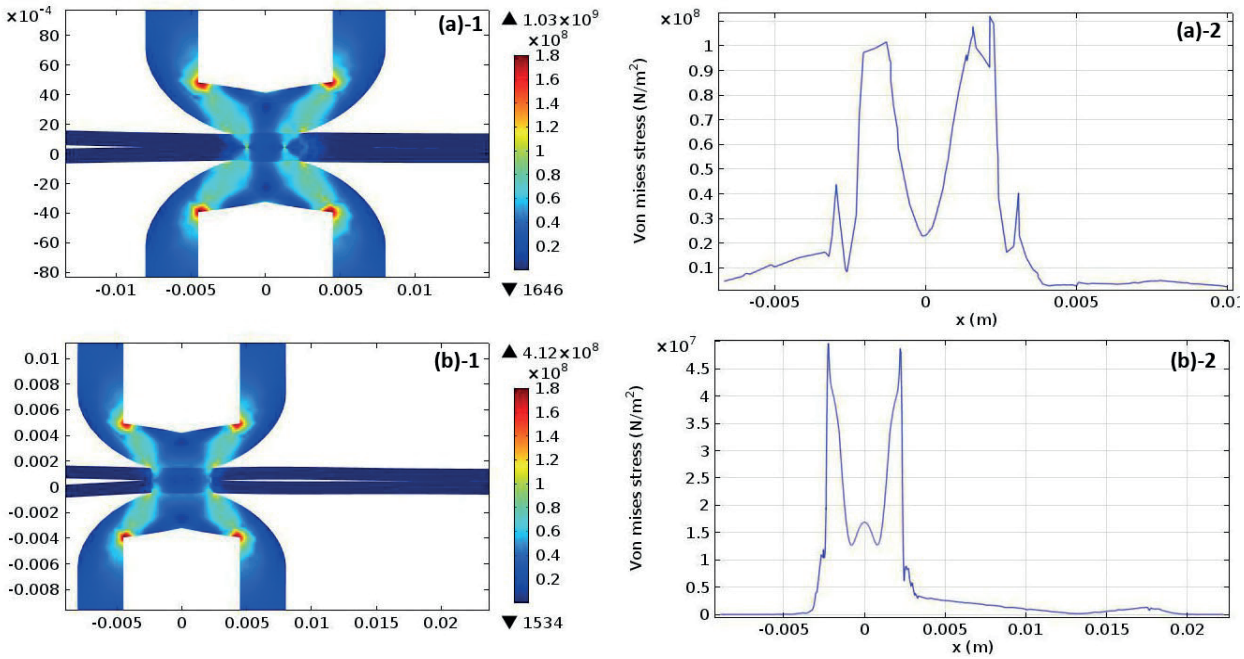

Fig. 15. Predicted stress distribution and deformations during the application of welding force at faying surface of shunted spot, with 23.5 kA welding current and 6 cycles welding time for (a) 5 and (c) 20 mm (magnification of deformation = 20x)

heating/cooling rates. In addition, Comparing diagrams (a) and (b) in Fig. 13 proves two contradictory effects. Changing the distance from 5 to 20 mm yields to a temperature difference of 500 and 600 K, respectively, between 11 to 15 cycles at $x = 0$ while it is decreased for HAZ. The main reason is the reduction of shunting effect in longer distances, which enhances the heat generation at faying surface. Heating rates are identical for both distance in Fig. 14.1, while they differ significantly in cooling rates between nuggets in Fig. 14.2. This is an important reason behind the tendency of HAZ geometry toward the shunting nugget. This issue is further discussed in section 3.2 and compared with micrographs.

3.2.3. Predicted stress distribution. Fig. 15 indicates predicted deformations and stress distributions. Shunting spot behaves as a barrier in front of deviations of sheets. This constraint has become weaker for longer distance (Fig. 15b). As a general rule, increasing welding distance adds to deformation and deviation of sheets, whereas it reduces stress value between the spots. This is a reasonable result since the shunting nugget acts as a mechanical constraint.

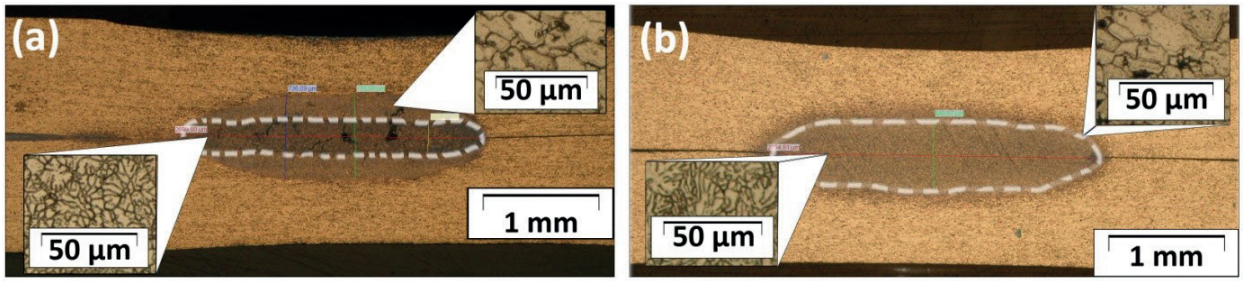

Fig. 16. Section of welding nugget produced by 22.5 kA welding current, 6 cycles welding time, and (a) 5, (b) 20 mm weld spacing (magnifications: macrostructure 25 x, microstructures 500 x; dashed curve is the approximate border of nugget and HAZ)

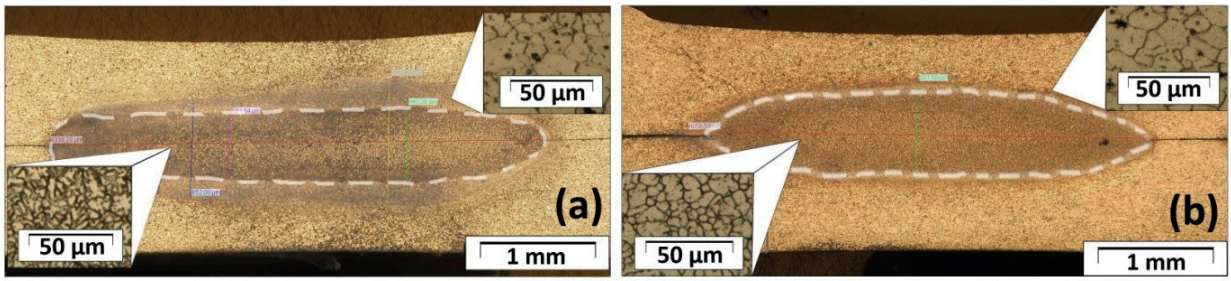

Fig. 17. Section of welding nugget produced by 25.3 kA welding current, 6 cycles welding time, and (a) 5, (b) 20 mm weld spacing (magnifications: macrostructure 25 x, microstructures 500 x; dashed curve is the approximate border of nugget and HAZ)

3.2. Nugget dimensions. Micrograph and dimensions of shunted nuggets are considered and compared to numerically predicted dimensions. Comparison of Fig. 16a and 16b indicates the reduction of nugget size, while HAZ size has grown toward previous spot due to shunting effect. This means a larger part of thermal energy is used for generating HAZ rather than nugget, while the size of HAZ in Fig. 16b is not considerable comparing to nugget dimensions. The same conclusion is true for Fig. 17, however the asymmetry is clearer here. In other words, the tendency of HAZ toward the previous spot is stronger than in Fig. 16; this is due to higher welding current and heat generation. Although welding distance in Fig. 16b and 17b is 20 mm, shunting effect is not observable due to weak shunting current for this distance.

Overall, Figs. 16 and 17 indicate the stronger effect of shunting current on reduction of nugget height than that of its diameter. This is also proved by numerical results as reduction in nugget height is easily comparable in Fig. 18a and 18b. In addition, extending HAZ toward the shunting welding nugget rather than the opposite side is reasonably proved by comparing numerical (Fig. 13 and 14) and experimental (Fig. 16 and 17) results, as it is numerically predicted in the form of temperature distribution required to generate HAZ.

3.3. Microstructure. The most important result drawn from SEM images concerns the segregation of alloying elements along grain boundaries, which is severe in HAZ. Segregation is intensified by increasing welding distance, as seen in Fig. 19 and 20. White areas indicate the concentration of alloying elements. Significance of concentration for 5 mm welding distance is higher than 20 mm. The same result is observed for segregation of copper in Fig. 21. Bright particles are representative of copper element in Fig. 21. It could be interpreted as the negative effect of shunting current on HAZ. In fact, shunting current has increased the nonuniformity of distribution of elements over HAZ. The main reason can be a rise of heat in HAZ acquired by shunting current which did not melt the HAZ, but altered the microstructure in a negative way.

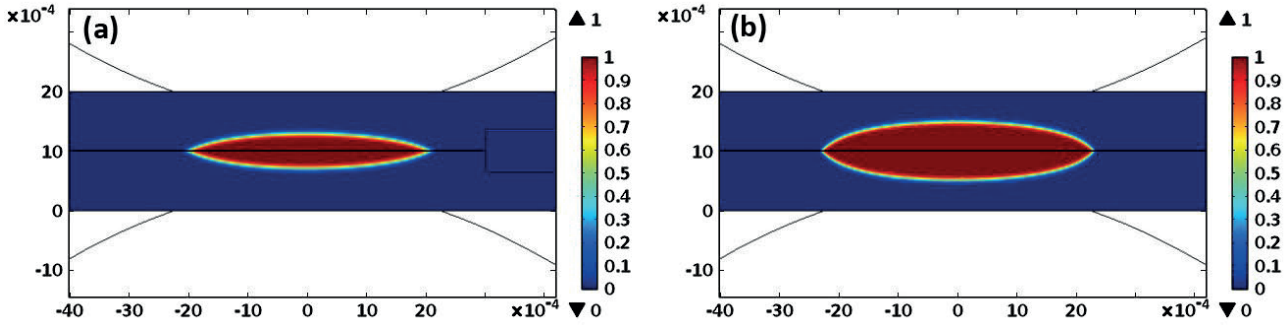

Fig. 18. Maximum predicted liquid phase ratio before removing welding current, for 25.3 kA welding current and 6 cycles welding time for (a) 5, (b) 20 mm welding distance

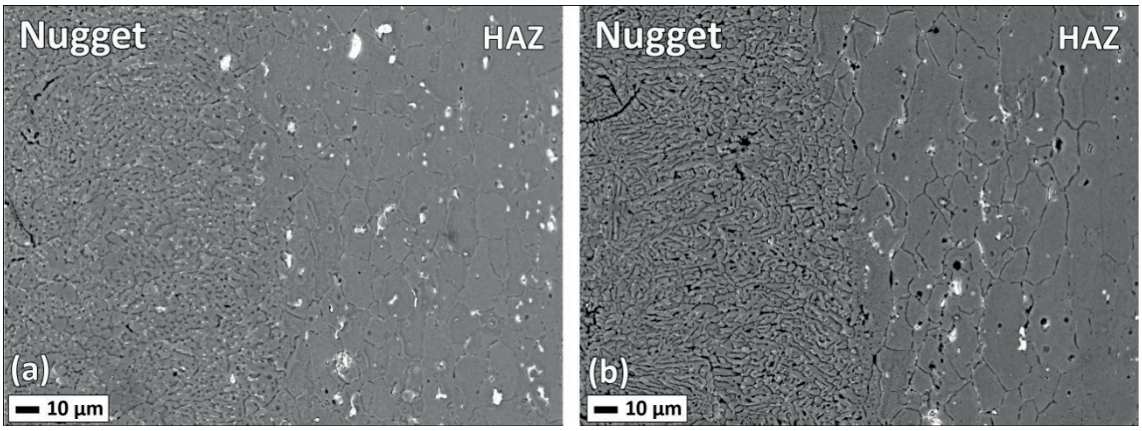

Fig. 19. SEM photo for the nugget section made by 25.3 kA welding current, 6 cycles welding time, and (a) 5, (b) 20 mm welding distance, with 500 x magnification

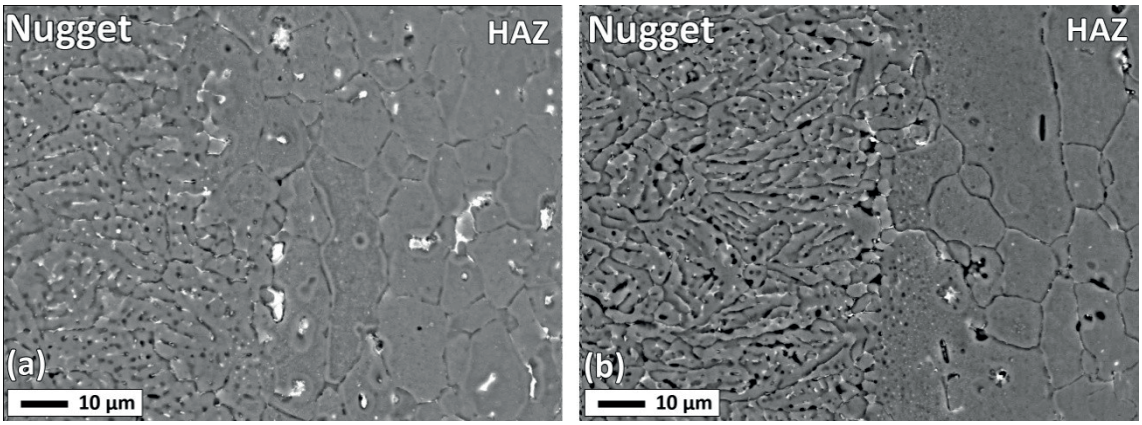

Fig. 20. SEM photo for the nugget section made by 25.3 kA welding current, 6 cycles welding time, and (a) 5, (b) 20 mm welding distance, with 1000 x magnification

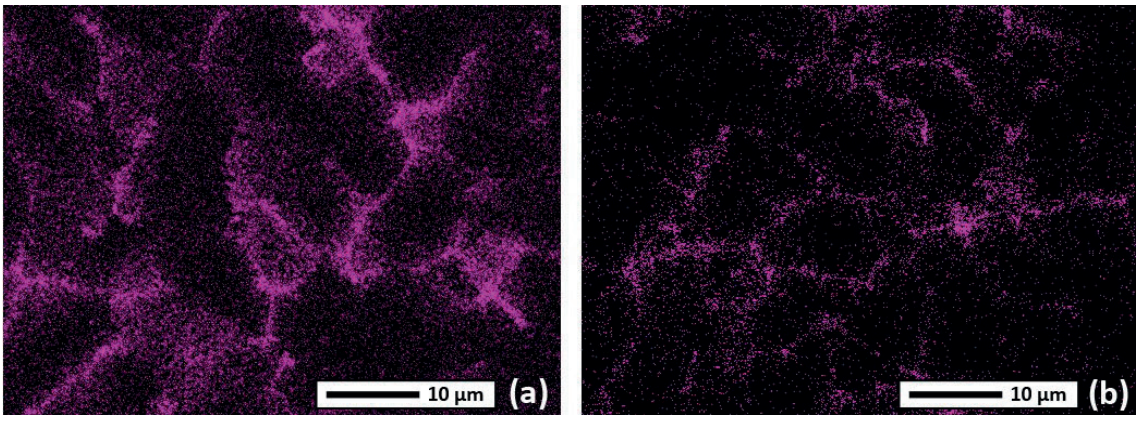

Fig. 21. Copper distribution in HAZ, made by 25.3 kA welding current, 6 cycles welding time, and (a) 5, (b) 20 mm welding distance, with 2000 x magnification

4. Conclusion

Shunting effect in resistance spot welding of 1 mm AA2219 sheets was considered experimentally and numerically using a finite element model for two adjacent spots. Weld spacing together with welding current and time were considered in a three factor DOE in experimental phase, while temperature dependence of material properties was respected in FEM. The following conclusions are drawn from the investigation of results:

- Numerical and experimental results are in appropriate agreement; however, some discrepancies are observed due to small difference between real and defined values of contact and shunting nugget properties.

- Distance effect was clearly observable on nugget size for experimental and numerical results. The main reason is the reduction of shunting current by increasing distance.
- The interactive effect of welding current and distance was clearly observed for diameter but it was very subtle for height.
- Voltage distribution prediction proved the effect of shunting on reduction of generated voltage at faying surface due to higher electrical conductance of shunting nugget.
- Stress distribution analysis indicated the effect of shunting spot on deviations and generated stress between spots. Increasing weld spacing reduced the maximum value of distributed stress, whereas it increased the deviation and separation of sheets between spots.
- Experimental and numerical investigation of nugget section proved the effect of shunting on nugget dimensions, particularly on height. Furthermore, HAZ asymmetry was observed in micrographs for shorter distances, while it was predicted by numerical results in the form of asymmetry in temperature values and cooling rates between spots.
- SEM images indicated the effect of shunting current on segregation and concentration of alloying elements along the boundaries of grains, particularly on HAZ domain.

References

[1] A. R. Hard, "Preliminary test of spot weld shunting in 24ST Alclad", *Welding Journal* 27 (6), 491–495 (1948).
[2] H. S. Chang and H. S. Cho, "A Study on the Shunt Effect in Resistance Spot Welding", *Welding Journal* 69, 308–316 (1990).
[3] P. Howe, "Spot weld spacing effect on weld button size", Sheet Metal Welding Conference VI, *AWS Detroit Section*, Paper C03, (1994).
[4] B. Wang, M. Lou, Q. Shen, Y. B. Li and H. Zhang, "Shunting effect in resistance spot welding steels – part 1: experimental study", *Welding Journal* 92 (6), 182s–189s (2013).
[5] J. Senkara and H. Zhang, "Cracking in spot welding aluminum alloy AA5754", *Welding Journal* 79, 194s–201s (2000).
[6] H. Zhang, J. Senkara and X. Wu, "Suppressing cracking in resistance welding AA5754 by mechanical means", *Journal of Manufacturing Science and Engineering* 129, 194s–201s (2002).
[7] Y. B. Li, B. Wang, Q. Shen, M. Lou and H. Zhang, "Shunting effect in resistance spot welding steels – part 2: theoretical analysis", *Welding Journal* 92, 231s– 238s (2013).
[8] H. Huh and W.J. Kang, "Electro-thermal analysis of electrode resistance spot welding process by a 3-D finite element method", *Journal of Materials Processing Technology* 63, 672– 677 (1997).
[9] N. Ma and H. Murakawa, "Numerical and experimental study on nugget formation in resistance spot welding for three pieces of high strength steel sheets", *Journal of Materials Processing Technology* 210, 2045–2052 (2010).
[10] J.A. Greenwood, "Temperature in spot welding", *British Welding Journal* 8 (6), 316–322 (1961).
[11] C.L. Tsai, O.A. Jammal, J.C. Papritan and D.W. Dickinson, "Analysis and development of a real time control methodology in resistance spot welding", *Welding Journal* 70 (12), 339s–351s (1992).
[12] T. Loulou, P. Masson and P. Rogeon, "Thermal characterization of resistance spot welding", *Numerical Heat Transfer Part B: Fundamentals* 49 (6), 559–584 (2006).
[13] J. Shen, Y. Zhang, X. Lai and P.C. Wang, "Modeling of resistance spot welding of multiple stacks of steel sheets", *Materials and Design* 32, 550–560 (2011).
[14] A. Nied, "The finite element modeling of resistance spot welding process", *Welding Journal* 63 (4), 123–132 (1984).
[15] J. E. Gould, "An examination of nugget development during spot welding, using both experimental and analytical techniques", *Welding Journal*, 1s– 10s (1987).
[16] W. Zhang, "Design and implementation of software for resistance welding process simulations", Journal of Material and Manufacture 112 (5), 556–564 (2003).
[17] J.H. Kim, Y. Cho and Y.H. Jang, "Estimation of the weldability of single-sided resistance spot welding", *Journal of Manufacturing Systems* 32, 505–512 (2013).
[18] M. Hamedi, H. Eisazadeh and M. Esmailzadeh, "Numerical simulation of tensile strength of upset welded joints with experimental verification", *Material & Design* 31, 2296–2304 (2010).
[19] X. Sun and P. Dong, "Analysis of Aluminum Resistance Spot Welding Processes Using Coupled Finite Element Procedures", *Welding Research*, 215S–221S (2000).
[20] COMSOL AB (2013). COMSOL Multiphysics – Heat Transfer Module Model Library Manual, Ver. 4.4, COMSOL AB ltd.
[21] H. Zhang and J. Senkara, *Resistance welding: fundamentals and applications*, CRC Press, UK (2006).
[22] Z. Hou, I. Kim, Y. Wang and C. Li, C. Chen, "Finite element analysis for the mechanical features of resistance spot welding process", *Journal of Materials Processing Technology* 185, 160–165 (2007).
[23] J. Sessler and V. Weiss, *Materials data handbook – aluminum alloy* 2219, 2nd ed., Western Applied Research & Development, CA (1966).
[24] E. L. Rooy, R.B.C. Cayless and J.W. Bray, *ASM handbook: properties & selection – nonferrous alloys and special-purpose materials*, 10th ed., Vol. 2, 3–165 (1990).
[25] MIL-HDBK-5H: *Metallic materials and elements for aerospace vehicle structures*, Chapter 3, 164–192, Department of Defense, USA (1998).
[26] M. Vogler and S. Sheppard, "Electrical contact resistance under high loads and elevated temperature", *Welding Journal* 72 (6), 231s–238s (1993).
[27] M. Jafari Vardanjani, M. Ghayour and R. Mokhtari Homami, "Analysis of the vibrational stress relief for reducing the residual stresses caused by machining", *Experimental Techniques* 6 (38), 1– 9 (2014).
[28] *Military Specification-Welding-Resistance: Spot And Seam, MlL-W-6858D, Department of the Air Force*, USA (1978).
[29] W.H. Kearns, *Metals and Their Weldability*, 7th ed., Vol. 4, American Welding Society Inc, FL, (1997).
[30] K. R. Chan, "Weldability and degradation study of coated electrodes for resistance spot welding", M.Sc. Thesis, University of Waterloo, Canada (2005).
[31] J. Saleem, A. Majid, K. Bertilsson, T. Carlberg and N. Ul Islam, "Nugget formation during resistance spot welding using finite element model", *World Academy of Science – Engineering and Technology* 67, 588– 593 (2012).
[32] *Procedure for spot welding of uncoated and coated low carbon and high strength steels*, Section 6, Document No. III-1005-93, International Institute of Welding.